

Chapter 2

Exact Theory of Optical Tweezers and Its Application to Absolute Calibration

Rafael S. Dutra, Nathan B. Viana, Paulo A. Maia Neto,
and H. Moysés Nussenzveig

Abstract

Optical tweezers have become a powerful tool for basic and applied research in cell biology. Here, we describe an experimentally verified theory for the trapping forces generated by optical tweezers based on first principles that allows absolute calibration. For pedagogical reasons, the steps that led to the development of the theory over the past 15 years are outlined. The results are applicable to a broad range of microsphere radii, from the Rayleigh regime to the ray optics one, for different polarizations and trapping heights, including all commonly employed parameter domains. Protocols for implementing absolute calibration are given, explaining how to measure all required experimental parameters, and including a link to an applet for stiffness calculations.

Key words Optical tweezers, Optical trap forces, Absolute calibration

List of Symbols

a	Radius of trapped particle
F	Trapping force
h	Distance from microsphere center to coverslip
k_z, k_ρ	Axial and transverse trap stiffness, respectively
λ, λ_0	Generic and vacuum wavelength, respectively
NA	Objective numerical aperture
n	Generic refractive index
n_g, n_p, n_w	Refractive indices of glass, trapped particle and water, respectively
OT	Optical tweezers
P	Incident laser beam power
Q_z, Q_ρ	Axial and transverse dimensionless efficiency factors, respectively
θ_o	Focused laser beam opening angle
ω	Laser beam angular frequency
z_{eq}	Axial equilibrium position

1 Introduction

In the preceding chapter, the history, design, and approximate theory of optical tweezers (OT) are introduced and discussed. In the present chapter, we outline the formulation of a theory based on first principles and its application to an absolute calibration, including instructions for how to measure all required experimental parameters. For indirect calibration methods, *see* refs. [1, 2] and references therein.

Why should one seek an absolute calibration? A basic rationale is to seek a full understanding of the physics of trapping forces, enabling one to predict the quantitative behavior of generated forces in various circumstances. Other benefits are possible design improvements and an extended spatial range of applicability.

In typical applications in cell biological and biophysical experiments, a TEM₀₀ near infrared laser beam (vacuum wavelength λ_0) goes through a beam expander and is focused by a high numerical aperture (NA) oil immersion objective of an inverted microscope, through a glass coverslip, into a water-filled sample chamber, to trap a transparent microsphere (radius a). Usually, λ_0 is neither $\gg a$ (Rayleigh range) nor $\ll a$ (ray optics range) so that neither the Rayleigh nor the ray optics approximation is appropriate. We therefore developed a theory based on first principles that permits an accurate calibration of OTs even in cases where λ_0 and a are similar. The theory is based on an optical (electromagnetic) representation of the highly focused laser beam produced by the objective and includes the defocusing effects of the glass/water interface (interface spherical aberration), and effects resulting from optical aberrations. To be of use in practice, its implementation must also provide procedures for the experimental determination of all requisite parameters.

Taking into account the wave diffraction phenomena associated with the physical processes described above, we are able to formulate an exact theory. For example, to calculate the forces acting on the microsphere, we employ the Mie scattering theory, which is an exact solution of the electromagnetic scattering problem [3, 4], and use Debye's exact representation of a converging beam in free space, which is based on a superposition of plane waves in all directions θ within the beam solid angle (angular spectrum of plane waves) [5]. However, to be of practical use, we will require its electromagnetic generalization, describing diffraction of the incident laser beam by the microscope objective.

This diffraction effect is treated by classical diffraction theory. This is a very good approximation in the domain to which it will be applied [6]. We exemplify this, for simplicity, by scalar diffraction by an aperture A in an opaque plane screen S (Fig. 1).

Rayleigh's formula [7] yields an exact result for the diffraction amplitude in the direction defined by unit vector $\hat{\mathbf{s}}$,

$$f(\hat{\mathbf{s}}) = \frac{\hat{\mathbf{s}} \cdot \hat{\mathbf{s}}_0}{i\lambda} \int \exp[-ik(\hat{\mathbf{s}} - \hat{\mathbf{s}}_0) \cdot \mathbf{x}] u(\mathbf{x}) d^2x, \quad (1)$$

where $\hat{\mathbf{s}}_0$ defines the direction of incidence, $k = 2\pi/\lambda$ is the wave number, the integral is extended over the full plane of the screen \mathbf{S} , and $u(\mathbf{x})$ is the (generally unknown) *exact* wave function on this plane.

For short wavelengths $\lambda \ll D$, where D is the aperture diameter, and for not too large diffraction angles θ (i.e., not $\gg \lambda/D$), we have in the domain where $|u(\mathbf{x})|$ is appreciable,

$$k(\hat{\mathbf{s}} - \hat{\mathbf{s}}_0) \cdot \mathbf{x} \leq kD \sin \theta = k_{\perp} D \text{ not } \gg 1, \quad (2)$$

where k_{\perp} is the transverse wave number. Thus, for not too large diffraction angles for which the intensity is mostly concentrated, the diffraction pattern reflects only Fourier components of the aperture distribution associated with broader features, rather than very fine details.

Classical diffraction theory is based on Kirchhoff's approximation. Applying Eq. 1 to the plane immediately beyond the screen (depicted by the dashed line in Fig. 1), Kirchhoff's approximation replaces $u(\mathbf{x})$ by the incident wave over the aperture A and sets it to vanish over the geometrical shadow, the blocked part of the screen S (shadowed area in Fig. 1). For not too large diffraction angles defined by Eq. 2, this blocking effect is a good approximation, explaining why classical diffraction theory works so well; in the

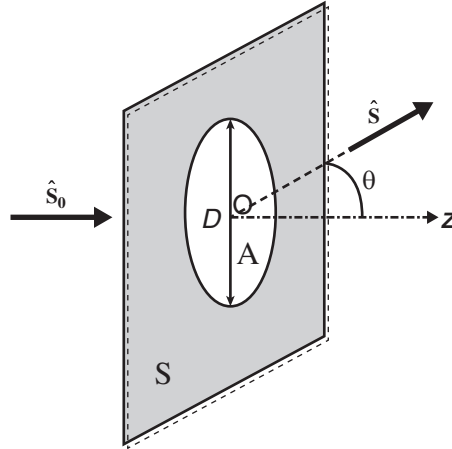


Fig. 1 Diffraction by an aperture on an opaque plane screen. On a plane immediately beyond the screen (shown by the *dashed line*), Kirchhoff's approximation replaces the wave function by its geometrical optics distribution (incident wave beyond the aperture and zero in the shadow region blocked by the opaque screen)

forward direction, the average of $u(\mathbf{x})$ over the aperture dominates the amplitude. This insensitivity of classical diffraction patterns to fine details in the aperture distribution is related to the principle of stationary phase and to stationary properties of the patterns [6].

1.1 Mie–Debye Approximation to the Axial Force

We outline the theory of absolute calibration as it was developed by successive approximations, incorporating new features as their needs were recognized. The first attempt was for the simpler case of the axial force, disregarding aberrations [8]. It employs Mie theory and represents the focused beam by the Richards and Wolf electromagnetic generalization [9] of the Debye model based on classical diffraction theory, which we call MD (Mie–Debye) approximation. Importantly, the Abbe sine condition [9] is taken into account.

The beam is generated by an incident Gaussian TEM₀₀ mode overfilling the microscope high NA objective (circular aperture), producing the diffracted highly focused beam. Each plane wave in this angular spectrum is Mie scattered by the microsphere, the center of which is aligned with the beam axis, defined as the z direction, leading to an axial trapping force. This force F can be obtained by computing the Maxwell stress tensor for the total (incident + scattered) field and integrating over the surface of the microsphere. It is usually expressed in terms of a dimensionless efficiency factor Q_z , the ratio of F to one half the force $2P/v$ exerted on a perfectly reflecting mirror by a perpendicularly incident light beam of power P in a medium of refractive index n , where $v = c/n$,

$$Q_z = \frac{cF}{nP}. \quad (3)$$

The result [8] is a partial-wave series in terms of the Mie coefficients. For size parameters $\omega a/c \gg 1$, where ω is the laser beam angular frequency and a is the microsphere radius, one finds that the efficiency factor at the position of the geometrical focus ($z = 0$) is asymptotically given by

$$Q_z(z = 0) = \frac{8r \sin^2(\Delta/2)}{1 + r^2 - 2r \cos \Delta} \langle \cos \theta \rangle \quad (4)$$

where $\Delta \equiv 4n_p \omega a/c$, n_p is the microsphere refractive index, and the angular brackets denote an average over the intensity distribution of the focused laser beam. This expression has a simple physical interpretation. It represents the radiation pressure efficiency factor of an infinite set of Fabry–Perot interferometers of width $2a$, refractive index n_p , and with round-trip phase Δ , each one oriented at angle θ , traversed at normal incidence by the respective angular spectrum component [10]. This near-sinusoidal oscillatory behavior was the first wave interference effect found in OT performance [11]. While its direct observation would demand a hard-to-attain

resolution, a closely related effect has been observed with water droplets trapped by a supercontinuum laser source [12].

At an axial equilibrium position z_{eq} , the axial stiffness is given by

$$\kappa_z = -\frac{n_w P}{c} \left(\frac{\partial Q_z}{\partial z} \right)_{z=z_{\text{eq}}}, \quad (5)$$

in which n_w is the refractive index of water in which the microsphere is immersed. In the geometrical optics limit, Q_z only depends on the dimensionless parameter $\zeta \equiv z/a$, so that

$$\frac{\partial Q_z}{\partial z} = \frac{1}{a} \frac{dQ_z}{d\zeta}. \quad (6)$$

In this limit, the stiffness must therefore decay hyperbolically as a function of the microsphere size a , which provides an important validation test.

Plotting the predicted κ_z versus a , one finds [8] the expected cubic power law growth in the Rayleigh region ($\omega a/c \ll 1$), going through a peak at $\omega a/c \approx 2.5$, followed by an oscillatory decay for $\omega a/c \gg 1$, where the small interference oscillations follow the pattern of the oscillations in Eq. 4. Averaging over the oscillations, one recovers the geometrical-optic hyperbolic decay (Eq. 6). This is the typical expected behavior of the (semiclassical) limiting transition from wave optics to geometrical optics [10].

1.2 MDSA Approximation to the Transverse Force

The next step in the development of absolute calibration was to extend the results to the transverse trapping force (relevant for cell biology applications), which began with a direct extension of the axial approach [13]. The microsphere center is no longer on the beam axis and the efficiency factor is a vector \mathbf{Q} , with (Q_ρ, Q_ϕ, Q_z) being the vector components in cylindrical coordinates. The transverse stiffness was first evaluated for circular polarization of the incident beam, and later extended to linear polarization [14].

The essential check that the partial-wave series expansions yield the correct results in the geometrical-optic limit is highly nontrivial, requiring the derivation of WKB (Wentzel–Kramers–Brillouin) approximations for the rotation matrices (Appendix B in [13]). An important feature of the transverse force evaluation was that the equilibrium position in the presence of a transverse pulling force was obtained by solving an implicit equation expressing the condition of a vanishing Q_z .

The results for the transverse trap stiffness as a function of microsphere radius a were similar to those for the axial case, showing growth to a peak followed by oscillatory decay, with size average over the oscillations asymptotically approaching the geometrical-optic results. Few experimental results were available at the time [13] was published, but they indicated a sizable

displacement of the peak position. This was attributed to neglect of interface spherical aberration, which stretches the paraxial focus into an axial strip and increasingly degrades the trapping force as one moves away from the interface.

The effects of interface spherical aberration on the Richards and Wolf representation of the focused beam were treated in ref. [15]. The main effect is the introduction within the angular spectrum integral representation of an additional phase factor $\exp(i\Psi)$, where

$$\Psi(z, \theta) = kL \left(\cos \theta_1 - \frac{\cos \theta}{N^2} \right). \quad (7)$$

is the interface spherical aberration function, L is the distance between the interface and the paraxial focal plane, $N = n_w/n_g$, where n_w and n_g are the refractive indices of water and glass, respectively, and $\theta_1 = \arcsin(\sin \theta / N)$ is the angle of refraction on the interface. The microsphere center coordinates are (ρ, ϕ, z) , with origin at the paraxial focus. One must also multiply the integrand by the Fresnel transmission amplitude, here given for perpendicular polarization,

$$T(\theta) = \frac{2 \cos \theta}{\cos \theta + N \cos \theta_1}. \quad (8)$$

The dependence of $T(\theta)$ on polarization is neglected, since N is close to unity, so that the results for parallel and perpendicular polarizations are very close.

Introducing these additional factors into the angular spectrum components and the associated terms of the partial-wave expansion, we get the MDSA approximation. The transverse trap stiffness κ_ρ is determined by

$$\kappa_\rho = -\frac{n_w P}{c} \left(\frac{\partial Q_\rho}{\partial \rho} \right)_{z=z_{\text{eq}}}, \quad (9)$$

where the axial equilibrium position z_{eq} is obtained by solving the implicit equation $Q_z(z_{\text{eq}}) = 0$.

A thorough experimental test of the MDSA approximation was performed independently by two laboratories using OT setups with an underfilled and an overfilled objective lens, respectively [16]. The experimental results show good agreement with the MDSA predictions, over a broad bead size range, for the following features:

1. *Trapping threshold.* For the case of an underfilled objective, the minimum bead size that can be trapped is signaled by a scattering of the experimental results over a range of different values (no stable equilibrium position).

2. *Location of the stiffness peak*, which is very sensitive to beam shape.
3. *Trap stiffness variation with height*, arising from interface spherical aberration.
4. *Multiple equilibria*. Although OT forces are in general not conservative, forces along the axis may be derived from an optical potential [17]. By plotting this potential for a typical configuration, one finds that the most stable axial equilibrium position changes with the height, and that the bead may hop between them as the objective is displaced. This is quantitatively confirmed by the experiment. In spite of these successful accomplishments, the MDSA approximation fails badly just at the stiffness peak, where the observed value is about $\frac{1}{4}$ of the predicted one. This was ascribed to additional optical aberration effects not included in MDSA [16].

1.3 MDSA+ and Absolute Calibration

Absolute calibration was finally achieved (*see Note 1*) by taking into account additional aberrations of the optical system [18], arising from the microscope objective and from other elements, such as the beam expander. The diffraction theory of optical aberrations [19] is employed to deal with them. They represent corrections to the Gaussian paraxial theory, which assumes that propagation angles θ around the beam axis are $\ll 1$.

The Seidel aberrations (the primary optical aberrations) introduce new phase corrections, associated with the lowest powers of an expansion in terms of $\sin\theta/\sin\theta_o$, where θ_o is the opening angle of the laser beam. Two of them, field curvature and distortion, do not affect the intensity distribution around the focus and can therefore be ignored. We refer to [18] for a systematic treatment of the other aberrations, as well as for images of some typical aberration effects. It reveals that coma does not strongly affect the trap stiffness and the system spherical aberration only introduces a correction to the interface spherical aberration discussed in the Methods Sect. 3. However, astigmatism has a very strong effect in the neighborhood of the stiffness peak, so that it is essential to take it into account.

This requires a diagnostic procedure to determine the astigmatism parameters. The method employed is an adaptation of that described in ref. [20]. Instead of being directed to the sample chamber after going through the microscope objective, the laser beam is reflected by a plane mirror placed near the focal plane. The laser light travels back through the objective, beam splitter and microscope tube lens to produce a recorded image for analysis. The relation with the astigmatism parameters is based upon Kirchhoff's approximation and the principle of stationary phase (see also the comments following Eq. 2).

Introducing the correction phase factors originating from optical aberrations into the MDSA approximation, one obtains the

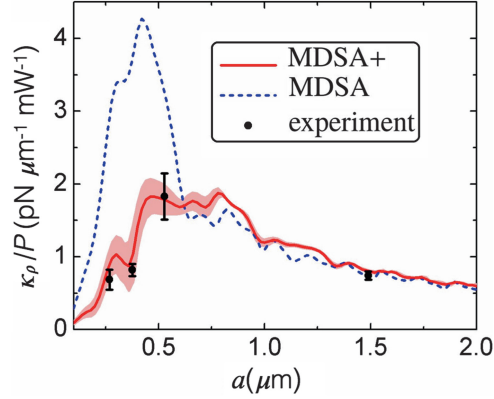


Fig. 2 Transverse OT stiffness per unit power κ_ρ/P vs. microsphere radius a for an objective lens displacement $d = 3.0 \pm 0.5 \mu\text{m}$. No adjustable parameters are employed. *Solid red line*: MDSA+ with measured astigmatism parameters $A_{\text{ast}} = 0.56 \pm 0.03$ and $\phi_{\text{ast}} = 55 \pm 5^\circ$. The *red shaded* theoretical uncertainty band is bounded by the curves for A_{ast} , ϕ_{ast} , and d , with their respective uncertainties. *Black circles*: experimental points. *Blue dashed line*: MDSA

“MDSA+” result for the trap stiffness (Appendix A in [18]). Comparison with experimental results for the transverse trap stiffness [18] shows that it corrects the MDSA overestimate of the peak height by a factor of order 4 and leads to an overall agreement within error bars, with no fitting needed, for microsphere radii ranging from the Rayleigh domain to the ray optics one, for all polarizations and trapping heights commonly employed in cell biology. Typical results for the transverse trap stiffness per unit power as a function of bead radius are shown in Fig. 2.

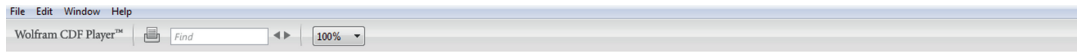
It also predicts a previously undetected window of instability around the peak region within a height range of a few microsphere radii. Indeed, plots of the axial optical potential at different heights show that it goes through a region of indifferent equilibrium. This is confirmed by experiment, which reveals appreciable dispersion of data taken within this region.

The height range where MDSA+ can be applied is bounded below, on account of some effects that are disregarded. They include optical reverberation (multiple light scattering between the microsphere and the interface), surface interactions, and contributions from evanescent waves beyond the critical angle [21]. For these reasons, it is not advisable to perform absolute calibration below distances of the order of the wavelength or the microsphere size from the interface.

2 Materials

An applet in Computable Document Format (CDF), for direct evaluation of the OT stiffness from experimentally measured input parameters, is described below. It contains instructions for its use and can be downloaded from <http://sites.if.ufrj.br/lpo/en> and employed after downloading the application Wolfram CDF Player (see **Note 2**).

The MDSA+ Applet for Absolute Calibration (Fig. 3) evaluates the axial equilibrium position, as well as axial and transverse optical trap stiffness values, for a microsphere of given radius, trapped by a circularly polarized laser beam, using MDSA+ theory [18]. Absolute calibrations require input data about the OT components and the optical setup, including the desired microsphere height above the coverslip, as well as seed values for numerical computations. It employs the MDSA+ partial-wave series for simulating the results for the calibration experiment: starting from the configuration with the trapped bead just touching the coverslip at the bottom of the sample chamber, one moves the objective lens upward by a desired distance d . The outputs of the applet are the height h of the actual equilibrium position (distance from the microsphere center to the coverslip) and the axial and transverse stiffness values, κ_z and κ_r . After entering the input parameters (see Methods Sect. 3), the following steps are internally performed:



Legend:

Blue: parameters to control the numerical calculations
 Red: parameters measured in the lab
 Brown: other important input parameters
 Black Bold: output parameters with 3 significant digits

$\alpha = -\log_{10}(\text{truncation error of Mie series})$	10
$L_0 = \text{initial seed for numerical root-finding algorithm that calculates the initial focal position, in units of microsphere radius}$	0
$z_0 = \text{initial seed for numerical root-finding algorithm that calculates the axial equilibrium position } h \text{ after objective displacement, in units of microsphere radius}$	0
$P_E = \text{laser power at objective entrance, in mW}$	100
$w = \text{waist of laser beam at objective entrance, in } \mu\text{m}$	4.2
$t = \text{mean transmittance of the objective}$	0.3
$A_{\text{un}} = \text{astigmatism parameter}$	0.1
$\phi_{\text{un}} = \text{astigmatism angle with respect to } x \text{ direction, in degrees}$	45
$d = \text{objective displacement, in } \mu\text{m}$	3
$\phi = \text{direction of microsphere displacement with respect to } x \text{ direction, in degrees}$	0
$R_{\text{obj}} = \text{radius of objective entrance, in mm}$	5.
$n_m = \text{refractive index of immersion medium (usually water)}$	1.332
$a = \text{microsphere radius, in } \mu\text{m}$	0.268
$\text{Re}(n_p) = \text{real part of microsphere refractive index}$	1.576
$\text{Im}(n_p) = \text{imaginary part of microsphere refractive index}$	0.001
$\lambda_0 = \text{laser wavelength in vacuum, in } \mu\text{m}$	1.064
$\text{NA} = \text{objective numerical aperture}$	1.4
$N_{\text{un}} = \text{number of terms retained in Mie series}$	4
$h = \text{equilibrium position height between the microsphere center and the glass slide surface, in } \mu\text{m}$	2.73
$\kappa_z = \text{axial trap stiffness, in pN}/\mu\text{m}$	8.52
$\kappa_r = \text{transverse trap stiffness, in pN}/\mu\text{m}$	73.5

Fig. 3 Picture of Applet for OT Calibration

1. Evaluation of the initial focal position L_i , imposing the equilibrium condition that the axial force vanishes when the microsphere touches the glass surface. Here the applet calculates the root of an equation involving partial wave series.
2. After performing an objective lens displacement d , evaluation of the corresponding equilibrium position height h , imposing again the equilibrium condition that the axial force vanishes for the new focal position $L = L_i + Nd$, where $N = n_w/n_g$. Here the applet calculates the root of an equation involving partial wave series.
3. Evaluation of axial trap stiffness κ_z .
4. Evaluation of transverse trap stiffness $\kappa_\rho(\phi)$, corresponding to the direction on the xy -plane defined by the azimuth angle ϕ chosen by the user.

To proceed, choose the seed values (L_0, z_0) required for the applet to perform the computation. The speed, and sometimes also the success of a computation, depends on how close the seed parameters are from the true root values. The seed parameter L_0 is employed to evaluate the initial focus position L_i , and z_0 is employed to evaluate the final equilibrium bead height h . Both are measured in units of microsphere radius. For a given microsphere radius a , L_0 is a fixed parameter and z_0 is a function of the objective lens displacement d (*see Note 3*).

All output values are given with three significant figures. For accuracy consistent with this number it is recommended to set the input accuracy control parameter α to $\alpha = 10$, as illustrated in Fig. 3. The computational time increases with α (*see Note 4*). It also increases with the microsphere radius a . For large microsphere sizes (far beyond those usually employed in biophysical experiments), convergence of the Mie series is slow, but geometric optics is then a good approximation.

3 Methods

In this section, we explain what data need to be collected as input parameters in order to employ the MDSA+ Applet for Absolute Calibration described in Materials Sect. 2, including instructions for how to obtain them. The required input parameters are listed below. For each of them, a protocol or a reference is provided.

1. Laser vacuum wavelength λ_0 : provided by the laser manufacturer.
2. Input beam waist w at the objective entrance. The laser is usually employed in a TEM_{00} spatial mode. This mode has a

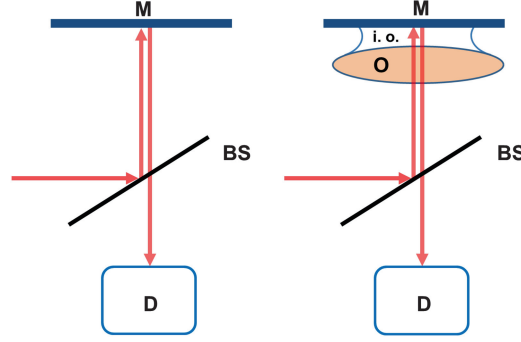


Fig. 4 Schematic representation of the measurement of the microscope objective's mean transmittance. *Left*: measurement without objective. *Right*: measurement with objective attached to mirror with immersion oil. *M* mirror, *D* Detector (power meter), *BS* Beam Splitter, *O* Objective, *i.o.* immersion oil

Gaussian intensity profile. Its waist w is determined by using a diaphragm and a power meter, measuring the laser power before (P_{in}) and after ($P(R_d)$) passing the diaphragm, as a function of the radius R_d of the diaphragm aperture [22], and fitting the results to Eq. 10:

$$P(R_d) = P_{\text{in}}[1 - \exp(-2R_d^2/w^2)]. \quad (10)$$

3. The refractive indices of water (n_w), glass (n_g), and of the trapped microsphere (n_p), at the temperature of the sample chamber, for vacuum wavelength λ_0 , which can be found in tables of physical constants. Microsphere absorption is represented by the imaginary part of n_p .
4. Microsphere radius a : provided by manufacturer (*see Note 5*).
5. The objective numerical aperture NA (provided by the manufacturer) and back entrance radius R_{obj} (measured using a caliper).
6. The laser power at the objective entrance P_E and the objective mean power transmittance t [16, 22]. The objective transmittance can be determined by a procedure inspired by the double lens method [23]: one employs a beam splitter (BS), a plane mirror (M), and a power meter (Fig. 4). A laser beam, with power P_{in} and radius R less than or equal to the objective entrance radius R_{obj} (to avoid overfilling), is first directed to the BS. The reflected part of the beam is then back-reflected by M at normal incidence and redirected to the BS. After passing through the BS (transmitted light), the power P_r is measured with the power meter. It is given by $P_r = r_{\text{BS}}t_{\text{BS}}P_{\text{in}}$, where r_{BS} and t_{BS} are the reflectance and transmittance of the BS, respectively (the reflectance of the mirror is assumed to be 100 %). The same procedure is then repeated, but now with the

objective lens placed in front of M, with a thin layer of immersion oil, to bring the objective lens and M in close contact (Fig. 4) (*see Note 6*). Finally, after passing through the BS, the power P_r' is measured. It is given by $P_r' = r_{BS} t^2 t_{BS} P_{in}$, with the transmittance t squared since the original beam now passes twice through the objective lens. The mean transmittance of the objective can then be obtained from the relation between P_r' and P_r : $P_r'/P_r = t^2$.

7. In the OT sample chamber, the trapped microsphere center is located at a distance h from the glass coverslip. The parameter h depends on the position of the system paraxial focus as well as on the sphere equilibrium position within the beam. The distance is experimentally determined by the following procedure. One traps a microsphere with the OT and one employs the microscope knob to determine when the microsphere touches the coverslip, by decreasing the distance between the surface of the trapped bead and the surface of the cover glass until the image of the microsphere undergoes a sudden large change [16]. This defines the microsphere radius a , since in this particular case $h = a$. Displacing the objective lens upward by a distance d , one reaches a height h that can be determined by employing the absolute calibration applet.
8. The primary aberrations of the optical system are astigmatism, coma, field distortion and spherical aberration. The microscope objective is built to avoid coma (*see Note 7*). Among the other three, only astigmatism and spherical aberration must be determined, since field distortion does not affect trapping stiffness. To verify whether the system has astigmatism, take a look at the focused laser beam by reflecting it on a mirror after passing through the objective, as in **step 6**. Astigmatic systems display two ellipsoidal spots at different axial positions. They can be observed [18] by slightly defocusing the system (Fig. 5) and are

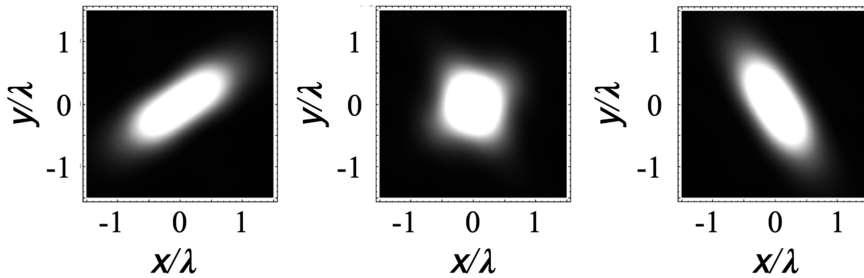


Fig. 5 Calculated energy density for three different planes along the optical axis in the presence of astigmatism with $A_{ast} = 0.4$ and $\phi_{ast} = 33^\circ$. Coordinates (x, y) define the position in the image plane and λ is the wavelength in the medium. The image in the *middle* corresponds to the *circle* of least confusion of an astigmatic system. The image on the *left* corresponds to the tangential focus and the image on the *right* to the sagittal focus

characterized by the amplitude A_{ast} and the angle ϕ_{ast} . They can be measured [18] by analyzing the reflected light intensity when the image of the spot is defocused near the focus of the optical system (*see* **Note 8**). If needed, the ellipsoidal spots can also be corrected by employing a spatial phase modulator [24, 25].

4 Notes

1. For a review of previous attempts to achieve absolute calibration, *see* ref. [16].
2. This application is freely available at the site: education.wolfram.com/cdf-player-download.html
3. Some reference values for the seed parameters L_0 and z_0 (in units of the microsphere radius) that optimize the numerical root-finding algorithm for typical OT setups are exemplified below. The values for z_0 are optimized for objective displacements d in the range from 3 to 5 μm . When employing larger values of d (so as to have a larger focal height), multiple equilibrium positions appear [16]. They can be found by using different seed values z_0 . Each root h represents a stable equilibrium position when the corresponding value found for the axial stiffness k_z is positive.

Example (1) $a = 0.27 \mu\text{m}$: $L_0 = 0.63$, $z_0 = -0.4$ (no astigmatism); $L_0 = -1.6$, $z_0 = 1.9$ (moderate astigmatism).

Example (2) $a = 0.53 \mu\text{m}$: $L_0 = 0.76$, $z_0 = -0.2$ (no astigmatism); $L_0 = -0.23$, $z_0 = 0.96$ (moderate astigmatism)

4. To illustrate typical computing times, the following numerical examples are based on the MDSA+ theory with the astigmatism parameters $A_{\text{ast}} = 0.56$ and $\phi_{\text{ast}} = 55^\circ$, the same used in ref. [18]. The α parameter was proposed in ref. [26] to control the number of Mie series terms retained and consequently the truncation error of the evaluation. The Wiscombe's criterion [27] is recovered for $\alpha = 15$. For a given α , the applet runs more slowly for large microspheres, because the number of Mie terms grows with microsphere radius. The calculations were performed using a standard notebook with an Intel® Core™ i5 processor and 8 Gb RAM. The average time spent with the applet to obtain h , κ_z and κ_ρ for four typical values of a with $\alpha = 10$, was:

Example (1) $a = 0.268 \mu\text{m}$: 9 s,

Example (2) $a = 0.376 \mu\text{m}$: 13 s,

Example (3) $a = 0.527 \mu\text{m}$: 20 s,

Example (4) $a = 1.49 \mu\text{m}$: 120 s.

5. For precision work, one can order NIST traceable microspheres.
6. One must ensure that, after reflection by M, the beam passes again through the objective lens and leaves it collimated, to recover the original beam as closely as possible, which can be done by adjusting the distance between M and the objective lens.
7. This can readily be checked by observing the image of the focused spot reflected by a mirror, noting the absence of coma features [18].
8. A simpler method to obtain a rough estimate of the astigmatism parameter is based on the measurement of the distance s between the tangential and sagittal foci around the diffraction focus [19]. This distance can be measured by displacing the mirror, using the microscope knob or a piezoelectric positioning system. A_{ast} is obtained employing a formula derived from the scalar diffraction theory of optical aberrations, valid in the paraxial regime ($\sin\theta_o \ll 1$) [19]:

$$s = 4 \left(\frac{A_{\text{ast}}}{\sin^2 \theta_o} \right) \lambda_g, \quad (11)$$

where λ_g is the laser wavelength in glass and θ_o is the objective angular aperture. The other important parameter to characterize the astigmatism is the angle, ϕ_{ast} , formed by the major axis of the ellipses that characterizes the astigmatic focus, with respect to the x axis, on the tangential focus region (*see* Fig. 4), first spot from left to right.

Acknowledgments

This work was supported by the Brazilian agencies CNPq, FAPERJ, and INCT Fluidos Complexos.

References

1. Neuman KC, Block SM (2006) Optical trapping. *Rev Sci Instrum* 75:2787–2809
2. Le Gall A, Perronet K, Dulin D et al (2010) Simultaneous calibration of optical tweezers spring constant and position detector response. *Opt Express* 18:26469–26474
3. Lorenz L (1890) Sur la lumière réfléchié et réfractée par une sphère (surface) transparente. *Kongel Danske Vidensk Selskabs Skrifter* 6:1
4. Mie G (1908) Beiträge zur Optik trüber Medien, speziell kolloidaler Metallösungen. *Ann der Phys (Leipzig)* 25:377–445
5. Debye P (1909) Das Verhalten von Lichtwellen in der Nähe eines Brennpunktes oder einer Brennnlinie. *Ann der Phys (Leipzig)* 89:755–776
6. Nussenzweig HM (1959) Diffraction theory in the k -representation. *An Acad Bras Cienc* 31:515–521, Reproduced in Oughston K E (editor) (1992) *Selected Papers on scalar wave diffraction*. SPIE Press, NY
7. Bouwkamp CJ (1954) Diffraction theory. *Rep Prog Phys* 17:35–100

8. Maia Neto PA, Nussenzveig HM (2000) Theory of optical tweezers. *Europhys Lett* 50:702–708
9. Richards B, Wolf E (1959) Electromagnetic diffraction in optical systems II. Structure of the image field in an aplanatic system. *Proc Roy Soc Lond A* 253:358–379
10. Nussenzveig HM (1992) *Diffraction effects in semiclassical scattering*. Cambridge University Press, Cambridge
11. Ashkin A (2006) Optical trapping and manipulation of neutral particles using lasers. World Scientific, Singapore, pp 201–202, 204
12. Guillon M, Dholakia K, McGloin D (2008) Optical trapping and spectral analysis of aerosols with a supercontinuum laser source. *Opt Express* 16(11):7655–7664
13. Mazolli A, Maia Neto PA, Nussenzveig HM (2003) Theory of trapping forces in optical tweezers. *Proc Roy Soc Lond A* 459:3021–3041
14. Dutra RS, Viana NB, Maia Neto PA et al (2007) Polarization effects in optical tweezers. *J Opt A Pure Appl Opt* 9:S221–S227
15. Török P, Varga P, Laczik Z et al (1995) Electromagnetic diffraction of light focused through a planar interface between materials of mismatched refractive indices: an integral representation. *J Opt Soc Am A* 12(2):325–332
16. Viana NB, Rocha MS, Mesquita ON et al (2007) Towards absolute calibration of optical tweezers. *Phys Rev E* 75:021914-1–021914-14
17. Roichman Y, Sun B, Stolarski A et al (2008) Influence of nonconservative optical forces on the dynamics of optically trapped colloidal spheres: the fountain of probability. *Phys Rev Lett* 101:128301-1–128301-4
18. Dutra RS, Viana NB, Maia Neto PA et al (2014) Absolute calibration of forces in optical tweezers. *Phys Rev A* 90:013825-1–013825-13
19. Born M, Wolf E (1999) *Principles of optics*, 7th edn. Cambridge University Press, Cambridge
20. Novotny L, Grober RD, Karrai K (2001) Reflected image of a strongly focused spot. *Opt Lett* 26:789–791
21. Schäffer E, Norrelykke SF, Howard J (2007) Surface forces and drag coefficients of microspheres near a plane surface measured with optical tweezers. *Langmuir* 23:3654–3665
22. Viana NB, Rocha MS, Mesquita ON et al (2006) Characterization of objective transmittance for optical tweezers. *Appl Opt* 45:4263–4269
23. Misawa H, Koshioka M, Sasak K et al (1991) Three-dimensional optical trapping and laser ablation of a single polymer latex particle in water. *J Appl Phys* 70:3829–3836
24. Roichman Y, Waldron A, Gardel E et al (2006) Optical traps with geometric aberrations. *Appl Opt* 45:3425–3429
25. López-Quesada C, Andilla J, Martín-Badosa E (2009) Correction of aberration in holographic optical tweezers using a Shack-Hartmann sensor. *Appl Opt* 48:1084–1090
26. Neves AAR, Pisignano D (2012) Effect of finite terms on the truncation error of Mie series. *Opt Lett* 37:2418–2420
27. Wiscombe WJ (1979) *Mie scattering calculations: advances in technique and fast, vector-speed computer codes*. Atmospheric Analysis and Prediction Division, National Center for Atmospheric Research, Boulder, CO

Optical Tweezers

Methods and Protocols

Gennerich, A. (Ed.)

2017, XII, 555 p. 154 illus., 133 illus. in color.,

Hardcover

ISBN: 978-1-4939-6419-2

A product of Humana Press